Winter PRIMER Ocean-Acoustic Solitary Wave Modeling Studies

Alex C. Warn-Varnas, Stanley A. Chin-Bing, *Member, IEEE*, David B. King, James A. Hawkins, Kevin G. Lamb, and James F. Lynch, *Fellow, IEEE*

Abstract—In this paper, we present results from a joint oceanographic-acoustic study of solitary waves and their effects during the 1997 winter PRIMER4 experiment on the shelfbreak south of Cape Cod, MA. The study addresses the acoustic effects induced by solitary waves and associated oceanographic phenomena. Solitary wave generation and propagation simulations are produced by the Lamb model [*J. Geophys. Res.*, vol. 99, pp. 848–864, 1994]. The model is nonhydrostatic and is formulated in 2.5 dimensions using terrain following coordinates. Acoustic field calculations are performed with a parabolic equation acoustic model along the path of solitary wave train propagation. The oceanographic model is initialized from density profiles derived from conductivity–temperature–depth (CTD) casts using analytical functions. The model is forced with a prescribed semidiurnal tidal velocity. An ocean background current is introduced. Simulations based on parameters derived from measurements show the following: 1) internal solitary waves of elevation propagate onto the shelfbreak region; 2) opposing ocean currents enhance the formation of solitary waves at the shelfbreak; 3) deepening of the winter mixed layer results in less penetration of the solitary waves on to the shelf; 4) density structure, mixed-layer depth, tidal forcing, and ocean currents control the formation of solitary waves of elevation at the shelfbreak; 5) energy conversion, from semidiurnal barotropic to semidiurnal barcoclinic tides and to internal solitary waves, occurs; 6) amplitudes and periods of modeled solitary waves are in the range of thermistor chain measurements; and 7) lower mixed-layer densities increase the phase speed of simulated solitary waves. Acoustic field calculations are coupled to the propagation of the solitary wave packets through the sound-speed changes that are derived from the oceanographic simulations. Acoustic model predictions show signal intensity fluctuations similar to the anomalous loses in acoustic energy observed in the Yellow Sea data taken by Zhou *et al.* [*J. Acoust. Soc. Amer.*, vol. 90, pp. 2042–2054, 1991]. In some cases, the presence of solitary waves on the shelf enhances the propagation of acoustic energy onto the shelf. This was observed for acoustic simulations where the acoustic source was located beyond the shelfbreak and at a depth greater than the shelf depth.

Index Terms—Continental shelf, internal waves, mode coupling, shallow water, shelfbreak front, solitary waves, sound propagation.

A. C. Warn-Varnas, S. A. Chin-Bing, and D. B. King are with the Naval Research Laboratory, Stennis Space Center, MS 39529 USA (e-mail: alex.warn-varnas@nrlssc.navy.mil).
J. A. Hawkins is with the Planning Systems Inc., Slidell, LA 70458 USA.
K. G. Lamb is with the University of Waterloo, Waterloo, ON N2L 3G1, Canada.
J. F. Lynch is with the Woods Hole Oceanographic Institution, Woods Hole, MA 02543 USA.

I. INTRODUCTION

SOUND propagation from the continental slope to the continental shelf is a complex problem. The effects on the acoustic field, as one progresses from the slope onto the shelfbreak, is a research issue of concern. In the winter of 1997, a field survey was conducted on the continental slope and shelfbreak south of Cape Cod, MA, in the Middle Atlantic Bight to address this problem. The survey was sponsored by the Office of Naval Research (ONR) and is part of the Shelfbreak PRIMER program from January 1995 through February 1997. The winter 1997 survey was referred to as PRIMER4 [1]. The program studied the effects of internal solitary waves, fronts, eddies, and seasonal stratification on acoustic propagation.

The shelf and slope water undergoes a large seasonal cycle in terms of vertical and horizontal stratification. There are complex interactions between the shelf, slope, and Gulf Stream waters [2]. Winter atmospheric forcing can result in deep mixed layer of around 100 m and a vertically mixed water column [3] over the shelf. The stratification strength decreases and the thermocline distributions descend to deeper depths relative to the summer conditions. The deeper locations of the thermocline influence the generation and propagation of internal solitary waves.

Internal tides are generated by the interaction of the barotropic tide with the winter stratification in presence of rapidly changing topography. Baines [4], [5] has demonstrated the generation process analytically. The tidally induced uplifting and depression of the isopycnals leads to the generation of internal solitary waves.

The temporal and spatial scales of tidally induced internal bores and solitary waves are such that they can have a significant effect on the acoustic field through the sound-speed structure. At certain frequencies, the interaction of the acoustic field with the solitary wave train can be quite significant. The resultant energy losses can be in the range of 5–15 dB depending on bottom assumptions [6], [7]. Sherwin [7] considered the effects of internal tides only. Zhou *et al.* [6] showed that the loss can by due to a solitary wave train by prescribing one through a gated sine function and deducing a transfer of acoustic energy from lower to higher modes.

The study of the interaction of the acoustic field with propagating solitary wave trains has become a research subject of concern. Preisig [8] investigated the coupling behavior of acoustic modes propagating through solitary wave trains. He found that the relative phase of acoustic modes propagating through the troughs of solitary wave trains control the net mode coupling induced by solitary wave trains. Duda [9], [17] showed that acoustic energy propagation through a solitary wave train is
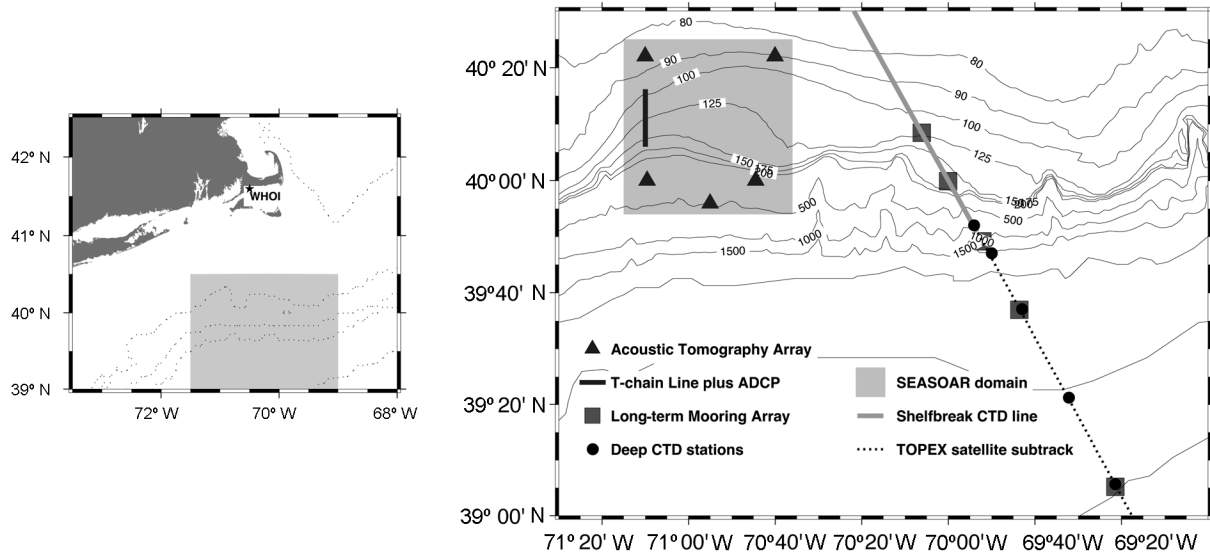
Fig. 1. Location and events for the winter PRIMER4 experiment conducted in February of 1997.

strongly influenced by the coupling of normal modes. He determined that the phasing within a propagating solitary wave train varies with time scales of minutes causing coupling and energy fluctuations. He also showed that acoustic energy loss can occur when mode coupling is from lower excited modes to higher modes. Gain of energy can occur when the coupling is from higher excited to lower modes. Finette [10] linked the acoustic field variability on the New Jersey continental shelf with the oceanographic field variability, dominated by internal solitary waves. In the linkage, he used a space- and time-dependent internal-wave model for shallow water. Rodriquez [11] studied the relationship between hydrographic and acoustic data from the INITMATE 96 experiment. He found that in presence of solitary wave trains there is an enhancement of the acoustic signal instead of attenuation. The enhancement behaved as a focusing effect and was attributed to nonlinear interactions.

In the Strait of Messina, we have demonstrated that in the presence of solitary waves the acoustic field can interact with the solitary waves and acoustic mode coupling can occur. This results in mode conversion with acoustic energy being redistributed from lower to higher modes and vice versa. When the converted modes have higher bottom attenuation than the original modes, higher signal loss can occur. At some frequencies, called resonance frequencies, the signal loss can be large enough to cause an appreciable drop in acoustic intensity [12].

This paper addresses the generation and propagation of solitary waves and their effects on the acoustic field during winter PRIMER4. This is a situation where internal solitary wave- trains of elevation propagate onto the shelf under a winter mixed layer. During summer PRIMER3, internal solitary waves of elevation were also observed on the shelf [13]. The paper is divided into sections on introduction, data, model, initial conditions, solitary wave modeling studies, acoustic studies, and conclusion.

II. DATA

The winter 1997 PRIMER4 survey (Fig. 1) was a joint physical oceanography and acoustics experiment sponsored by ONR

Deployed	2/17/97 0827 (Z)
Recovered	2/26/97 1755 (Z)
Latitude N	40° 14.4889'
Longitude W	71° 09.9965'
Depth	104 m
Sampling Interval	4 s

TABLE I
FAST SAMPLING THERMISTOR CHAIN

Thermistor	Depth (m)
t-pod #958	1
#1	26
#2	27
#3	28
#4	30
#5	32 (did not work)
#6	36 (did not work)
#7	40
#8	44 (did not work)
#9	52
#10	60 (did not work)
#11	68
#12	84
#13	100
#14	101
t-pod #956	102

involving a group of institutions. The objectives of the data gathering were oriented toward the study of the thermohaline variability and structure of the shelfbreak front and its effects on acoustic propagation. The mesoscale field was surveyed with SeaSoar hydrography, shipboard acoustic Doppler current profiler (ADCP), satellite sea surface observations, and aircraft-deployed expendable bathythermograph (AXBT) drops. Internal solitary waves and the finer scales were surveyed with rapid-sampling thermistor chains, current meters, and an upward looking ADCP. The acoustic component consisted of 400-Hz transceivers, a 224-Hz source, and hydrophone arrays. Fig. 1 indicates the locations of the measurements. A fast-sampling thermistor chain tracked the internal waves and solitary internal waves. It was positioned on the western edge at a depth of 104 m (Table I). The spatial sampling extended from 26 to 101 m.

III. MODEL

The Lamb [14] model is used for simulating the generation and propagation of internal solitary waves in the PRIMER region. It consists of the inviscid incompressible Boussinesq equa-
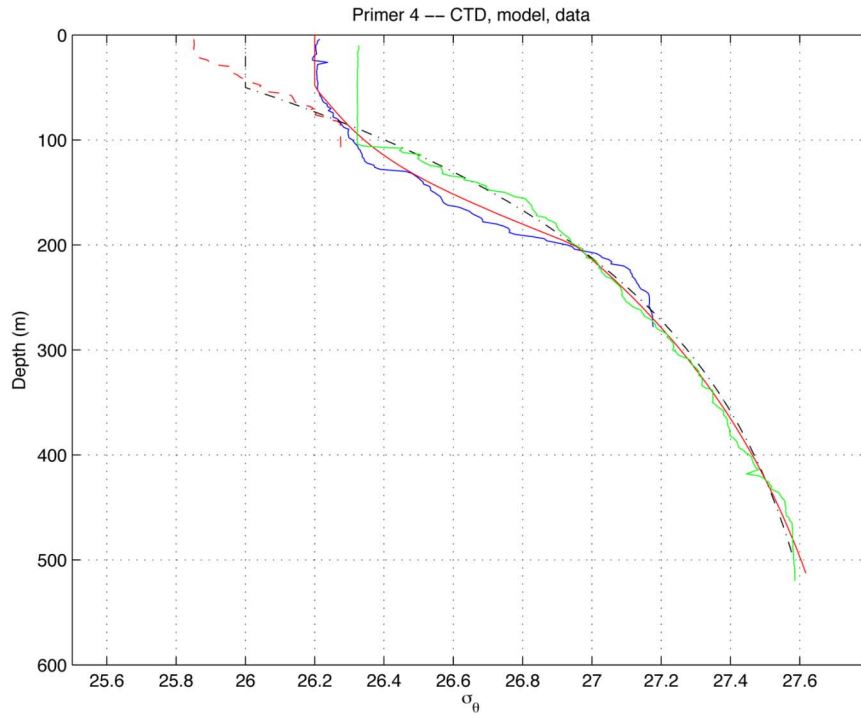
Fig. 2.   Density from CTD casts and fitted profiles. Dashed red, blue, and green (squares, triangles, and stars) represent CTD casts. Black dot-dash (circle) is case 1 of Table II fitted profile and solid red curve (asterisk) is case 6 of Table II fitted profile.

tions on a rotating f-plane. In the along-bank direction (i.e., y-direction), the velocity v is included, however, the derivative with respect to the y-coordinate is neglected (hence, the designation "2.5 dimensional" representation). The equations of the model are

$$V_t + V \cdot \nabla V - fV \times \hat{k} = -\nabla P - \hat{k}\rho g \qquad (1)$$
$$\rho_t + V \cdot \nabla \rho = 0 \qquad (2)$$
$$\nabla \cdot V = 0 \qquad (3)$$

where $V(u, v, w)$ is the velocity vector, ∇ is the three-dimensional (3-D) vector gradient operator, subscript t denotes the time derivative, ρ is the density [14] from the fluid density term $(1 + \rho)$, P is the pressure, g is the gravitational acceleration, f is the Coriolis parameter taken as 9×10^{-5} s^{-1} for a latitude of $40°$, and $\hat{k}$ is the unit vector along the z-direction [refer to the coordinate axes shown in Fig. 3(a)]. In the 3-D (1)–(3), the partial derivatives with respect to y are neglected, i.e., $\partial/\partial y(\cdot) = 0$; thus, (1)–(3) are equivalent to [14, eq. (1a)–(1d)].

Before the equations are solved, they are transformed to a terrain following coordinate system (sigma-coordinates), which leads to higher vertical resolution over the bank region. The equations are solved over a domain bounded below by the topography and a rigid lid above. The flow is forced by specifying the semidiurnal tidal velocity on the left boundary as

$$u_{bc} = V_T \sin(\omega t + \phi) \qquad (4)$$

where V_T is the semidiurnal tidal magnitude, ω the tidal frequency, and ϕ the phase factor.

A stretched grid is used outside of the region of interest. This results in the boundaries being sufficiently far away that wave reflection is not a problem.

IV. INITIAL CONDITIONS

The density field for model initialization was derived from CTD surveys along tracks in the region. One of the tracks was on the western edge where the thermistor chain was located. Another track was on the eastern side. Some of the CTD casts and constructed density profiles are shown in Fig. 2. The casts exhibit mixed-layer depths from about 20–110 m with a range of densities. Shallower casts further up on the shelf, in the upper 80 m show mixed-layer densities ranging from 25.5 to 26.2 sigma–theta (σ_θ).

We fitted exponential and hyperbolic secant (sech) profiles to the densities derived from data on the western end, using the observations at 50, 200, and 500 m.

The functional form of the fit is

$$\sigma_\theta = a + be^{-z/c} + d\,\text{sech}(qz). \qquad (5)$$

In some cases, the hyperbolic sech was fitted between 50–200 m with the two parameters selected to match the slope and range of the data [red (asterisk) curve in Fig. 2]. In other cases, the exponential fit was used [black dash-dot and red (circle and asterisk) (below 200 m) in Fig. 2]. A 50 m mixed layer with a σ_θ of 26.0 was chosen as a representative shelf value based on CTD casts and thermistor chain data [black dash-dot (circle) curve (case 1 in Table II) in Fig. 2]. This particular fitted curve has an exponential only that follows the CTD cast shown by the green (star) curve in Fig. 2, and then continues on until the 50-m

Case	MLD (m)	MLD σ_θ	sech	V_b (m/s)	V_g (m/s)
1	50	26	no	0.3	0.1
2	50	26	no	0.3	0
3	50	26	no	0.15	0.1
4	50	25.8	no	0.3	0.1
5	50	26.2	no	0.3	0.1
6	50	26.2	yes	0.3	0.1
7	70	26.3	no	0.3	0.1

MLD is the mixed layer depth, V_b the prescribed barotropic velocity on the left boundary, V_g the prescribed geostrophic velocity magnitude, and sech is the hyperbolic secant function used in the analytical σ_θ construction.

mixed layer is reached. For some of the other CTD casts, the derived densities, from 50 to 200 m, deviate from the exponential fit in the form of a convex intrusion. Shallower CTD casts tended not to contain this intrusion. The deviation is attributed to a warm Gulf stream ring that impinges on the shelf during the survey. To represent its effects, we introduced a hyperbolic sech fit between 50–200 m [the solid red (asterisk) curve (case 6 in Table II) with a mixed-layer density value of 26.2 for σ_θ in Fig. 2]. The mixed-layer density was varied by decreasing it and increasing it (cases 4 and 5 in Table II). Mixed-layer depths were also varied from 50 to 70 m (case 7 in Table II).

East of the Shelfbreak PRIMER study area, a relative minimum in semidiurnal barotropic tidal strength occurs [13]. This is the area of the weaker subresonant response of the Mid-Atlantic Bight. Analysis of the summer PRIMER mooring data yielded a Major Axis of 9.7 cm/s and a Minor Axis of −7.2 cm/s with cross-isobath currents of 5–12 cm/s [13]. The Baroclinic M2 semidiurnal tidal component is bottom intensified and propagates onto the shelf with downward phase [13]. Using a maximum barotropic tidal velocity of 12 cm/s over a depth of 147 m yields a barotropic tidal velocity of around 30 cm/s at a depth of 60 m through mass flux conservation. This is the maximum tidal velocity that we used on the left boundary of the model (Table II).

A shelfbreak front is contained in the PRIMER area [13]. The frontal jet exhibits meandering variations and ranges in magnitude from 10 to 15 cm/s. The physical picture is further complicated by a warm core ring, shed off the Gulf Stream that impinged upon the shelf during the PRIMER4 survey [1].

The direction of the jet current can be off the shelf, in which case it reduces the effective group velocity of the tidally induced internal bore propagating onto the shelf. This allows more time for the steepening of the internal bore and enhances its disintegration into internal solitary waves. To represent this effect we introduced a geostrophic velocity directed off the shelf with a magnitude of 0.1 m/s at the left boundary (Table II) into the model. A potential flow field over the topography is solved for and used as the geostrophic flow in the model. It is approximately uniform in z.

V. SOLITARY WAVE MODELING STUDIES

The initial model simulation (case 1 in Table II) was initialized with the density profile represented by the black dash-dot curve in Fig. 2. This density profile was introduced throughout the horizontal domain [Fig. 3(a)]. The bathymetry was obtained from chirp sonar measurements along the ship tracks. The model was forced with a prescribed semidiurnal barotropic tidal forcing on the left boundary of magnitude 0.3 m/s varying with the semidiurnal tidal period (4). The prescribed ocean current was directed off the shelf with a magnitude of 0.1 m/s and was represented by introducing a geostrophic velocity into the model.

A. Dynamics

During off-shelf flow, the semidiurnal tidal forcing results in motion over the shelfbreak that depresses the isopycnals in the pycnocline at the shelfbreak. The depression results in a right- and a left-propagating wave. The right-propagating wave develops into a slight depression of the isopycnals, away from the shelfbreak, every semidiurnal tidal period. Over several semidiurnal tidal cycles it becomes visible [Fig. 3(d)]. At 18 h or about 1.5 semidiurnal tidal cycles, the second cycle of off shelf motion is in progress and a depression is formed that is visible just off the shelfbreak [Fig. 3(b)] (end of off-shelf flow that occurs during the first part of each semidiurnal tidal cycle). Twelve hours later, the depression moves to the left and another one is formed to the right of it [Fig. 3(c)], by the off-shelf flow. The new depression moves left and deepens as it moves. This basic generation and formation structure prevails on the shelfbreak throughout the semidiurnal tidal cycles. The two depressions of Fig. 3(c) continue their journey to the left and move onto the shelf while a new depression is formed to the right of them at 42 h [Fig. 3(d)]. There, on the shelf, the back side of the depression bores become steep through nonlinear effects while the leading edge flattens, leaving a bore of elevation. Frequency and amplitude dispersion sets in and disintegration into internal solitary waves occurs.

At 74 h [Fig. 3(e)], there are four solitary wave trains of elevation on the shelf. The first train that moved on the shelf from left to right is decaying. The decaying train is crawling into the vanishing space between the 50-m mixed layer and the shelf. The second and third trains are evolved and the fourth is in the growth phase. The decaying stage involves an increase in the spacing between the solitary waves and a decrease in their amplitude. 74 h represents about six semidiurnal periods. The spin-up time for the formation of internal solitary bores is around 1.5 semidiurnal tidal periods. As a result, 4.5 solitary wave trains of elevation can be expected at 74 h. This is the case in Fig. 3(e) with four trains on the shelf and the fifth beginning to form on the edge of the shelf. During the evolution process, a mode-two vertical structure appears at around −32 km. As this mode-two structure moves to the left, the internal solitary waves disappear in the water column and then reappear as a mode-one structure on the back edge side.

B. Parameter Variations

The parameters of Table II were deduced from the CTD casts (see Section IV). The CTD casts encompass an envelope for
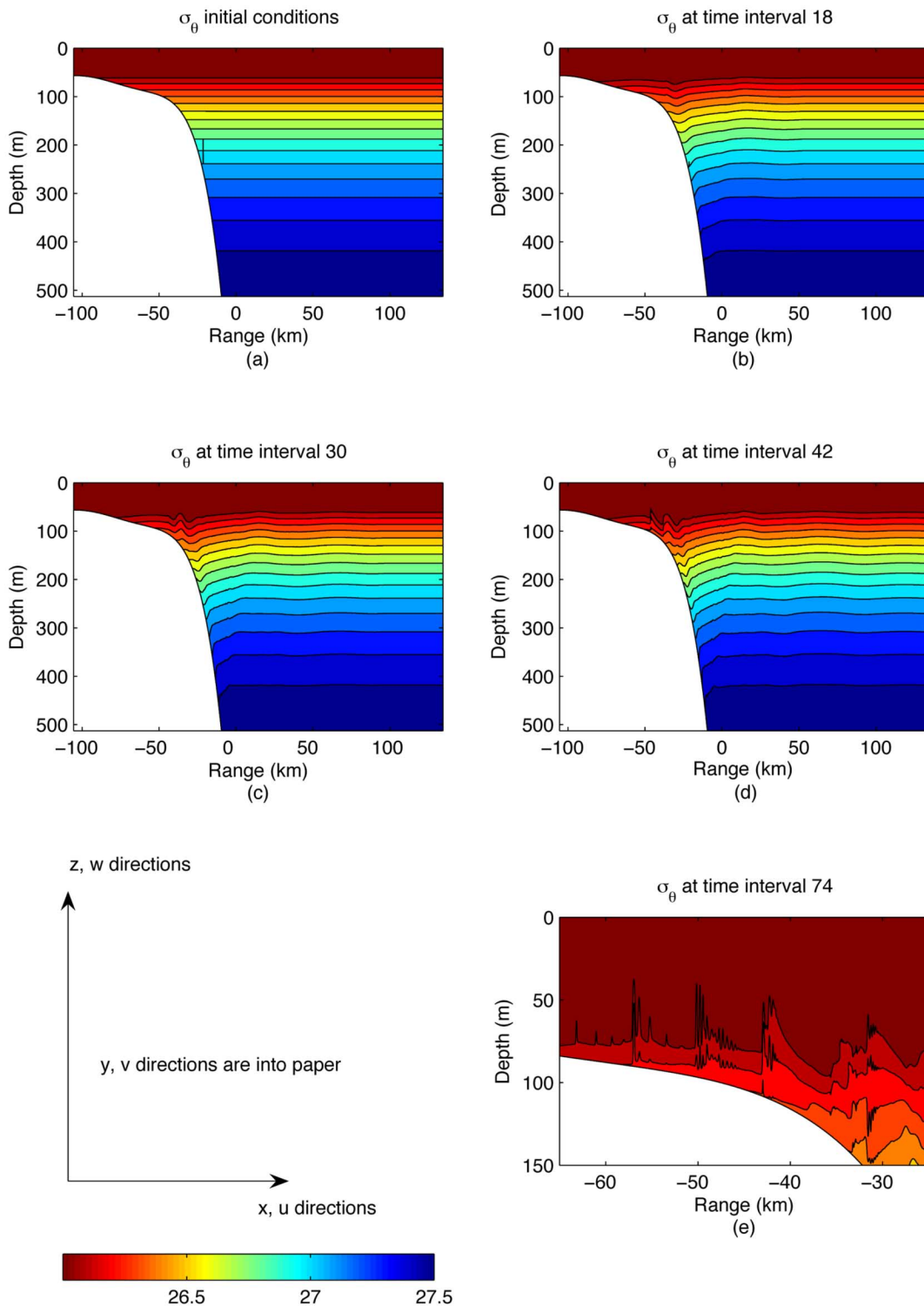
Fig. 3. Model simulated density fields for case 1 in Table II. (a) Initial density field. (b) Density at 18 h. (c) Density at 30 h. (d) Density at 42 h. (e) Density over the shelf and shelfbreak at 74 h. Bottom left graph indicates coordinates. The color bar underneath it shows the sigma–theta density scale.

density structure that exhibits variation. This variation is reflected in the parameters of Table II.

The solitary wave structure on the shelf of Case 1, in Table II, is shown in Fig. 4(a) at 57 h or 4.6 semidiurnal tidal periods. There are three developed solitary wave trains of elevation on the shelf, at around −55, −45, and − 40 km. The signature of these trains at the location of the thermistor chain measure-

ments are addressed in Section V-D that considers the comparison with thermistor chain observations. As the trains propagate toward shore, the widths of the solitary wave increase, the spacing between them increases, and the amplitudes decrease. At around −30 km, solitary wave trains of elevation (in the upper 80 m) and solitary wave trains of depression (below 90 m) have formed [Fig. 4(a)]. This reflects a mode-two vertical struc-
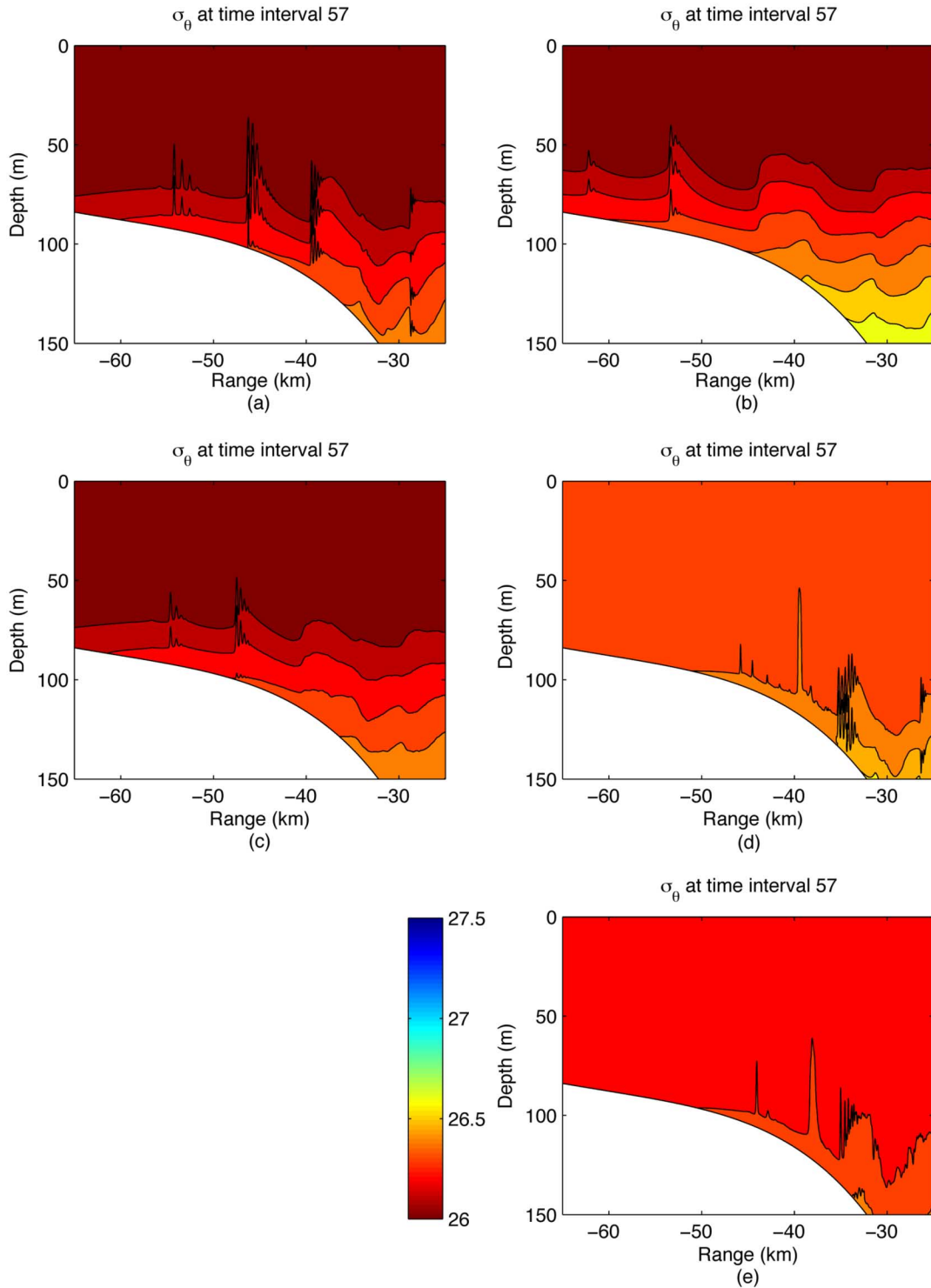
Fig. 4. Solitary wave train structures over the shelf region as a function of parameters. (a) Case 1 in Table II. (b) Case 2 in Table II. (c) Case 3 in Table II. (d) Case 7 in Table II. (e) Case 6 in Table II. The bottom left color bar shows the sigma–theta density scale.

ture. Proceeding onto the shelf, only the solitary wave trains of elevation that are formed on the back side of the depression bore prevail.

This case has a prescribed geostrophic current of 0.1 m/s (case 1 in Table II) directed off the shelf. Turning this current off (case 2 in Table II) results in the solitary wave structure shown in Fig. 4(b). The solitary wave trains and internal bores have moved further toward shore; the first train has advanced to around −63 km. There are, however, fewer solitary waves in the trains or no solitary waves at all. The offshore current retards the motion of the bore and trains. This gives more time for nonlinear effects to steepen the back edge of the bores. At this point, frequency and amplitude dispersions set in and disintegration into solitary waves occurs.

Decreasing the amplitude of the barotropic tidal forcing from 0.3 to 0.15 m/s (case 3 in Table II) yields the solitary wave and bore structure shown in Fig. 4(c). The amplitudes of the solitary waves have decreased and there are fewer of them, relative to case 1 in Fig. 4(a). At −40 km and −30 m, no solitary waves have formed at all. This suggests that reducing the barotropic forcing results in less internal bore displacement [14] and reduction in the nonlinear effects.

Cases 4 and 5 in Table II have a decrease and increase of density in the mixed layer relative to case 1. The resultant density structure has larger and smaller gradient in the pycnocline region. This leads to larger and smaller phase speeds for the internal solitary waves of elevation with slight enhancement (one more solitary wave toward the end of the train) of solitary waves for the larger gradient situation.

Case 7 in Table II has a mixed layer of 70 m that is larger than the 50 m in case 1. This reflects more winter mixing that penetrates further into the ocean and results in a larger mixed-layer depth. The isopycnal structure at 57 h is shown in Fig. 4(d). Relative to Fig. 4(a), the phase speed of the solitary waves is less and they are pushed further down on the shelf because of the deeper mixed-layer depth. Because of the deeper mixed-layer depth, there is less penetration of the solitary waves onto the shelf. The first train is more spread apart with larger distances between solitons than in Fig. 4(a). A large-amplitude solitary wave appears at around −40 km. This is the first solitary wave of the second train. The third train at around −35 km has more solitary waves than in Fig. 4(a). At around −25 km another train structure is forming and with a mode-two structure. The whole solitary wave train structure is pushed back to the right in relation to Fig. 4(a).

Case 6 in Table II represents a depression of the pycnocline that can be caused by warm Gulf Stream rings impinging on the shelf. The pushing down has an analogy, in the sense of a deeper pycnocline location, to the previous case with the 70-m mixed layer. Fig. 4(e) shows the results at 57 h. The first solitary wave train at around 45 km has fewer solitary waves than in Fig. 4(d). Only one solitary wave appears at the second train locations around 40 km with an enlarged width. This suggests a nonlinear dynamical effect that has a "resonance" behavior resulting in the formation of a large solitary wave. The third solitary wave train at around −35 km is still present. The mode-two solitary wave train structure has not formed at around −25 km. The solitary waves tend to be suppressed due to a deeper pycnocline location relative to the winter mixed-layer case shown in Fig. 4(a).

C. Spectral Variations at Mooring Lines

Comparisons of time series spectra were conducted between the thermistor chain data (Table I) and the corresponding observation posts in the model. Fig. 5 shows the mooring lines with observation posts placed in the model. The marks on the lines correspond to the sensor locations on the thermistor chain. The line marked C is the analogue of the thermistor chain in Table I. Line R is located 10 km to the right of C and line L is located 10 km to the left of C. Observation posts on the lines track the time progression of isopycnals and isotherms at the respective spatial locations. In the data (Table I), the 9° isotherm is tracked in time and in the model simulation the 26.1 σ_θ isopycnal.
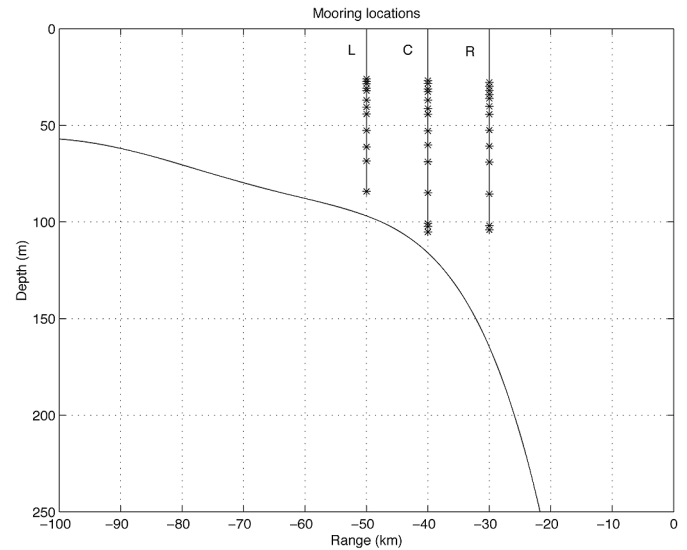

Fig. 5. Location of observations posts along mooring lines. Mooring C is at the thermistor chain location, Table I. The stars represent the sensor or observation post locations. Mooring line R is 10 km to the right of C, and mooring line L is 10 km to the left of C.
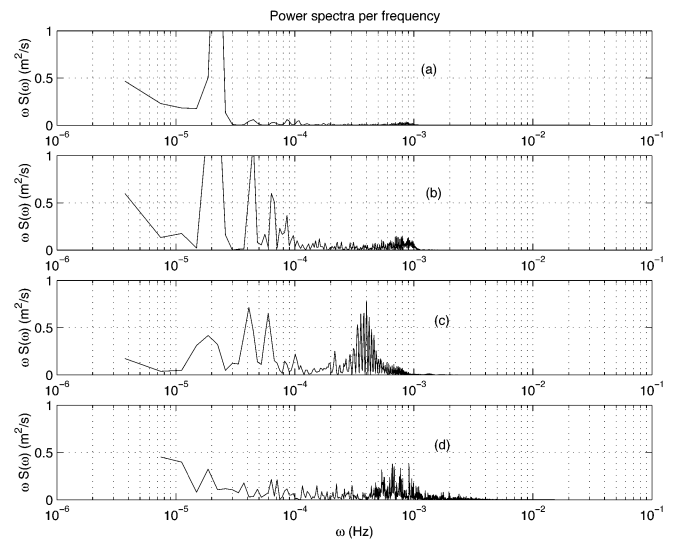

Fig. 6. Computed spectra. Variance spectra computed from model simulations and data. Model simulation time series track the $29.1\sigma_\theta$ isopycnal over a period of 3.08 d. Data time series track the 9° isotherm obtained from data for Julian days 51.5 through 54.5. (a) Variance spectra of model simulations at mooring line R. (b) Variance spectra of model simulations at mooring line C. (c) Variance spectra of model simulations at mooring line L. (d) Variance spectra of data at mooring line C.

The spectral analysis of the data from Julian day 51.5 to Julian day 54.5 is displayed in Fig. 6(d) in terms of variance spectra. Correspondingly, the model spectra for the time period of the simulations 3.08 days is shown in Fig. 6(b) at the analogue thermistor chain location of Table I, mooring line C in Fig. 5. Fig. 6(a) and (c) shows the results for displacements to the right (line R in Fig. 5) and to the left (line L in Fig. 5). The model is initialized from rest, spun up, and then the internal solitary waves evolve. In Fig. 6(b) and (d), both spectra exhibit internal solitary wave activity peaks around a frequency
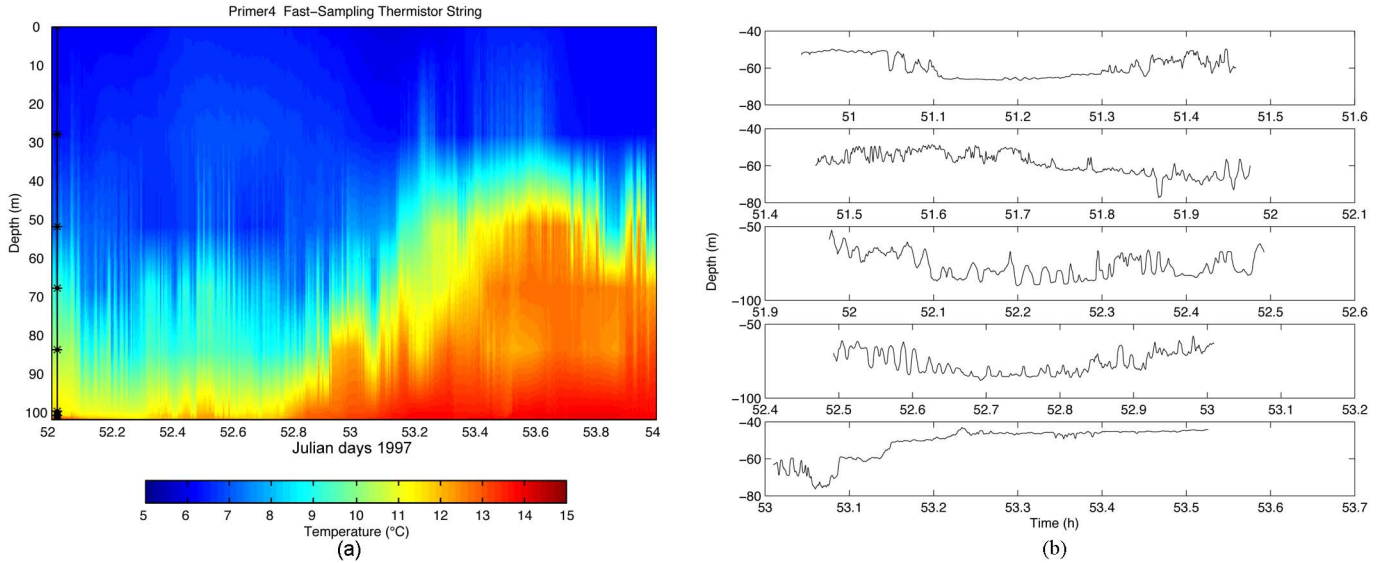
Fig. 7. (a) Temperature as a function of depth and time observed by the thermistor chain sensors from Julian day 52 through 54. (b) Detailed span of observed 9° isotherm depth and time from Julian day 50.95 through 53.53.

of 10^{-3} s^{-1}. Both spectra peaks overlap around the internal solitary wave frequency of 10^{-3} s^{-1} with a broadening of the variance data spectra. The broadening suggests the presence of larger and smaller internal-wave periods relative to the mean frequency or period distribution. The span of frequencies is from about 0.5×10^{-3} s^{-1} to 1.5×10^{-3} s^{-1} or equivalently a span of periods from 0.55 to 0.18 h. The modeled internal solitary wave energy is not as broad around the frequency of 10^{-3} s^{-1}. The span of frequencies is from 0.6×10^{-3} s^{-1} to 1.1×10^{-3} s^{-1} or over a span of periods from 0.46 to 0.25 h. The magnitude of the modeled internal solitary wave spectrum is smaller than the data while the magnitude of the spectrum at the semidiurnal tidal frequency 2.24×10^{-5} s^{-1} is much larger in the model results than the data. This we attribute to the spin-up time interval in the model results whereby internal bores are generated from which the internal solitary waves later appear. The modeled variance spectrum starts below the Brunt–Väisälä frequency and continues to somewhat below the semidiurnal tidal frequency of around 2.24×10^{-5} s^{-1}. The inertial oscillation is at around a frequency of 9×10^{-5} s^{-1}.

It is interesting to follow the progression of the model spectra on mooring lines R, C, and L (Fig. 5). On mooring line R there is a pronounced peak at the semidiurnal tidal frequency of 2.24×10^{-5} s^{-1} [Fig. 6(a)] and little energy around the solitary wave frequency of 10^{-3} s^{-1}. This indicates relatively more internal bore activity than internal solitary wave activity as the bore propagate up onto the shelf. At mooring line C [Fig. 6(b)] the internal solitary wave activity has increased while the internal bore activity is decreasing, less energy in the semidiurnal peak at 2.03×10^{-5} s^{-1} (peak value change is from 97.6 to 60.6). On mooring line L [Fig. 6(c)] the internal solitary wave activity has increased further and shifted to lower frequencies from 10^{-3} s^{-1}, indicating larger periods as the internal solitary waves of elevation propagate onto the shelf. The internal bore activity has decreased further, as evidenced by less energy at the semidiurnal

tidal frequency of 2.24×10^{-5} s^{-1}. The energy magnitude at the internal bore frequency has become comparable to the peak energy in the solitary wave band, similar in behavior to the data spectra [Fig. 6(d)].

The data shows relatively less energy at the semidiurnal frequency of 2.24×10^{-5} [Fig. 6(d)] than the corresponding model results at mooring C [Fig. 6(b)]. This suggests that the model results contain an appreciable spin-up interval during which there is conversion of semidiurnal tidal energy into internal bores and later conversion of internal bore energy into internal solitary wave energy, as shown in Fig. 6(c).

D. Comparisons With Thermistor Chain Observations

Table I lists the location of the thermistor chain and the distribution of the thermistors in depth. Some of them did not work. A plot of the data from Julian day 52 to 54 is shown in Fig. 7(a). The data exhibits oscillation due to internal solitary waves of elevation. Around Julian day 52.8 a warming trend starts in the lower layers and continues through Julian day 54. It is caused by the impingement of a warm Gulf Stream ring onto the shelf. A detailed display of the 9°C isotherm from Julian day 50.95 to 53.53 shows the propagation of internal solitary waves of elevation [Fig. 7(b)]. The structure of the internal solitary wave trains exhibit variability in amplitude and period. During sometime periods, the structure of the solitary wave trains is clearly identifiable (Julian days 52.18 to 52.29). Other times, the structure is more complex (Julian days 51.5 to 51.6). There are quiet periods when significant solitary wave activity is absent (Julian days 51.15 to 51.3).
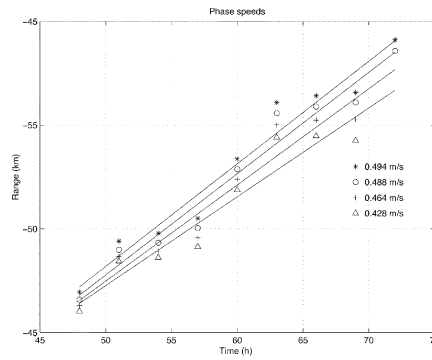
Model results, at the same mooring line as in Table I, show displacements of isopycnals in time that indicate the propagation of internal bores and solitary waves of elevation [Fig. 7(c)] where the $\sigma_\theta = 26.1$ isopycnal is shown. The time evolution of the model simulation contains a spin-up time during which the internal bores and solitary waves develop. The solitary wave
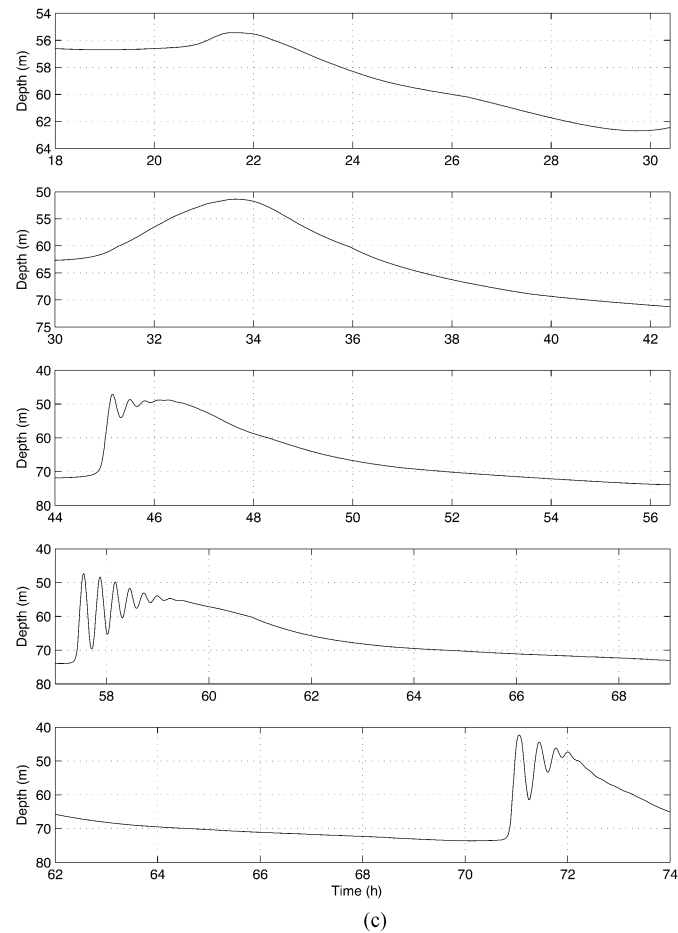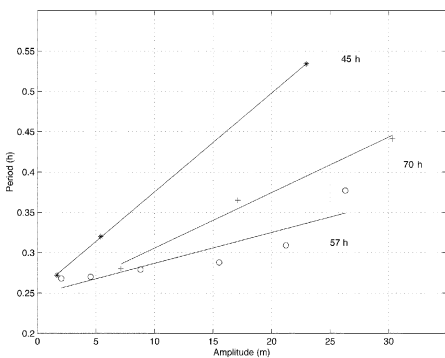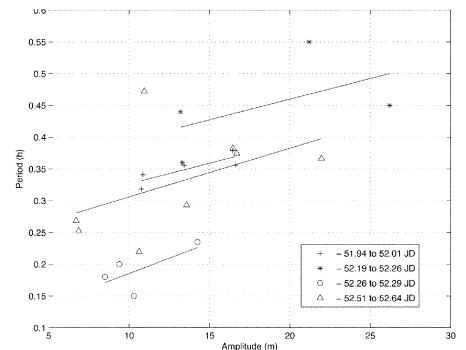
Fig. 7. (*Continued.*) (c) Modeled $\sigma_\theta = 26.1$ isopycnal for case 1 (Table II) as a function of depth and time. (d) Modeled solitary wave amplitude and period distribution at 45 h ($*$), 57 h ($\circ$), and 70 h ($+$). Solid lines are fitted curves. (e) Phase speeds for second solitary wave train for case 1 in Table II. The star indicates the first solitary wave, circle the second, plus the third, and triangle the fourth. Solid lines are least squares fits to the corresponding points. (f) Analyzed period versus amplitude behavior for measure solitary wave trains at the thermistor chain mooring. The analyzed time periods are as follows: "$+$" Julian days 51.94 to 52.01, "$*$" Julian days 52.19 to 52.26, "$\circ$" Julian days 52.26 to 52.29, and "$\triangle$" Julian days 52.51 to 52.64. Solid lines are least squares fits to the corresponding points.

trains start developing at around 45 h into the simulation. Near 57 h the solitary wave train is more developed than at 45 and 74 h and contains more solitons. This is the most evolved state of the solitary wave train. As the train moves past the observation posts, the isopycnals tend to return toward their equilibrium position within a semidiurnal tidal period.

E. Dispersion

The amplitudes and periods of the simulated internal solitary waves were extracted by placing points in the peaks and troughs and calculating the differences between them along the vertical and horizontal axes. The analysis is for the $\sigma_\theta = 26.1$ isopycnal that tracks the solitary wave trains at time spans near 45, 57, and 74 h [Fig. 7(c)]. The resulting dispersion diagram at the times of internal solitary waves of elevation is shown in Fig. 7(d). At 57 h, the amplitudes range from 27 to about 2 m and the periods (as observed at location) from about 0.35 h (21 min) to 0.26 h (16 min). The preceding solitary wave train at 45 h contains only two solitary waves of appreciable signature with the first exhibiting

the largest period 0.54 h (32min). The solitary wave train at 70 h has about three solitary waves of appreciable signature. The amplitudes of these solitary wave trains are comparable to those found at 57 h. The period variations from 0.26 to 0.45 h is in the range of the periods found in the analyzed spectra of data [Fig. 6(d)] where the period values range from 0.55 to 0.18 h.

The variation in internal solitary wave train structure at 74 h relative to 57 h at the observation site can be due to nonlinear dynamics, changing conditions induced by the succeeding solitary wave trains, and the influence on the dynamics of the prescribed offshore geostrophic velocity (Table II). It is possible that other variations of modeled solitary wave amplitudes and periods exist for different combinations of parameters in the parameter space.

The characteristics of the solitary waves in the second wave train to form and propagate onto the shelf were analyzed for phase speed behavior. The analysis was accomplished by placing points in the troughs and peaks of the solitary waves and tracking their behavior in space and time. A plot of the resultant time tracking is shown in Fig. 7(e), where the star refers to the first peak, plus the second, circle the third, and triangle the fourth. The lines represent least square fits that yield phase velocities ranging form 0.49 to 0.43 m/s. An inspection of the point behavior in time indicates intervals of small change in location (51–57 h) that result in small phase speeds and large change (57–63 h) that result in large phase speeds. Small changes occur when the tide is directed off bank and opposes the solitary trains on bank motion. Large changes occur when the tide is directed on bank and reinforces the solitary wave train on bank motion. These trends repeat themselves every 6.1 h as the semidiurnal tide reverses direction. The phase velocities vary with the direction of the tide. The variations are summarized in Table III. During the reinforcing part of the cycle the phase velocities vary from 0.93 to 0.8 m/s. During the opposing cycle they range from 0.18 to 0.04 m/s. As mentioned previously, the averages over both spans of the cycle range from 0.49 to 0.43 m/s.

The dispersion analysis of the observed solitary waves shown in Fig. 7(b) is exhibited in Fig. 7(f) for selected solitary wave train from the data. One analyzed set of data is from Julian day 52.19 through Julian day 52.29 and consists of a larger and smaller solitary wave train of elevation. In the larger solitary wave train the amplitudes range from 27 to 13 m and the periods from 0.55 h (33 min) to 0.35 h (21 min). The smaller train has amplitudes from about 15 to 8 m with periods from 0.23 h (14 min) to 0.15 h (9 min).

An analysis for an earlier time span consisting of Julian days 51.94 to 52.01 shows amplitude variations from 11 to 17 m. Then, corresponding periods range from 0.32 h (19.2 min) to 0.38 h (22.8 min).

In a later time span from Julian days 52.51 to 52.64, the amplitudes range from 7 to 22 m. The periods vary from 0.25 h (15 min) to 0.375 h (22.5 min). The extracted amplitudes and periods do not show a linear behavior in time. This can be due to nonlinear dynamics or more than one source of origin for the internal solitary wave trains.

The model result overlaps with the amplitudes and periods deduced from the measurement. This indicates that the model can predict the periods and amplitudes contained in the data. The overlap of the model simulation and the data occur over the internal solitary wave range of the spectra. The high-frequency tail end of the solitary wave spectra in the data is not observed in the model simulations. It could be due to noise.

VI. ACOUSTIC STUDIES

The acoustic effects of the solitary waves are simulated by applying a highly accurate ocean acoustic parabolic equation (PE) propagation model [15], the finite element parabolic equation (FEPE) model, to selected environmental "snapshots" generated by Lamb's model [14]. Collins' FEPE model was chosen rather than his latest PE model, range-dependent acoustic model (RAM), because FEPE allows greater user control over very wide propagation angles-fine grid structure tradeoffs; the much longer computational time required for the FEPE model as compared to the RAM model was not a determining factor. A series of sound-speed fields at one hour intervals were used for this simulation. The environments used for the acoustic simulations correspond to case 1 of Table I.

The placement of the source with respect to the internal wave can have a significant effect on the acoustics. To illustrate this, we will show the effects for two source depths. The first set of simulations was made using a deep-water location for the acoustic point source (at a depth of 125 m and at a range before the shelfbreak). Thus, the acoustic energy was propagated up and onto the shelf.

In one set of studies, the acoustic source frequency was fixed at 225 Hz. Acoustic energy was propagated onto the shelf through static ocean environments (i.e., "snapshots") created by the Lamb model at evolution times of 56, 57, and 58 h. The results are shown in Fig. 8(a) as color contour plots of acoustic transmission loss. The transmission loss at 56 h shows mode stripping as the acoustic field propagates into the shallower region of the shelf (i.e., the region shown on the far right of the 56-h panel, where only a two-mode structure survives). At 57 h the acoustic intensity (shown on the far right of the 57-h panel) has decreased below the background level, and at 58 h the acoustic energy reappears. The disappearance of acoustic energy at 57 h and reappearance at 56 and 58 h is suggestive of a temporal "resonance effect" [6] for the source frequency of 225 Hz.

Because this is a simulation study, one can try different "what if" situations. In one such "what if" simulation the sound-speed profiles were removed from the environment that represented the solitary internal-wave packet at the shelf break. The acoustic simulations for a frequency of 225 Hz and for a source at 0 range and 125-m depth [same parameters used for Fig. 8(a)] is shown in Fig. 8(b) for 56, 57 and 58 h. Notice that the "resonance effect" shown in Fig. 8(a) is not evident in Fig. 8(b), indicating that the presence of the internal wave is responsible for the loss seen in Fig. 8(a).

The effect of the presence of internal waves for 57 h as a function of frequency is shown in Fig. 9. This figure is a measure of the "integrated" internal-wave effect over the whole water column. A range of 85 km was selected and the intensity was
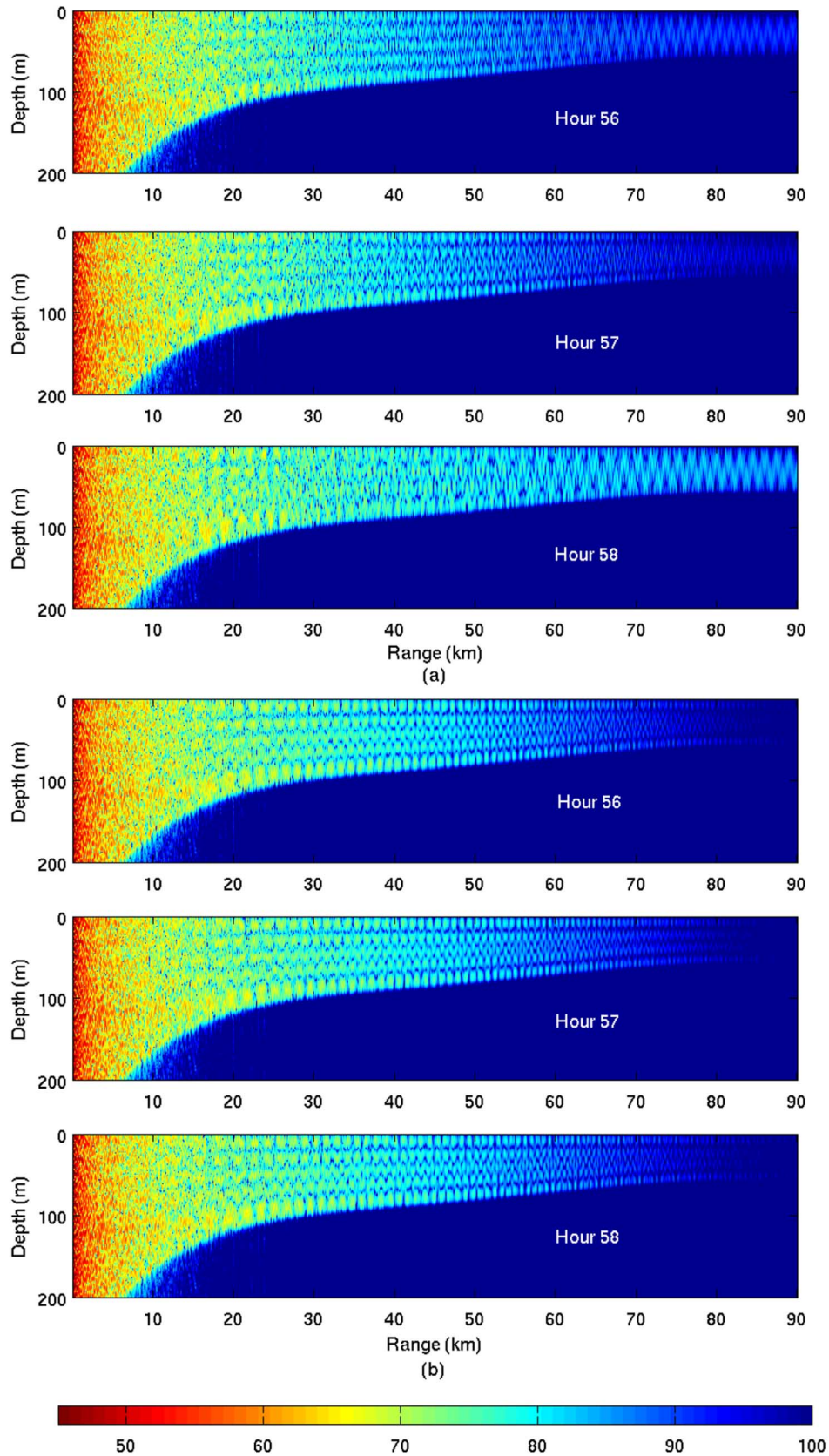
Fig. 8.   Acoustic response to the environment for 56, 57, and 58 h. The acoustics are shown as transmission loss as a function of depth and range. The acoustic source is 225 Hz and is located at range of 0 km and a depth of 125 m. The simulations with internal-waves present are shown in part (a) and the simulations without the internal waves are shown in part (b). It is evident in part (a) (with internal waves present) there is a loss of energy on the shelf for 57 h that is not evident for adjacent times, i.e., before and after 57 h. In part (b) (without the presence of internal waves), there is no evidence of energy loss. The shaded (color) scale represents the loss in decibels with black (blue) the most intense and white (red) the least intense.
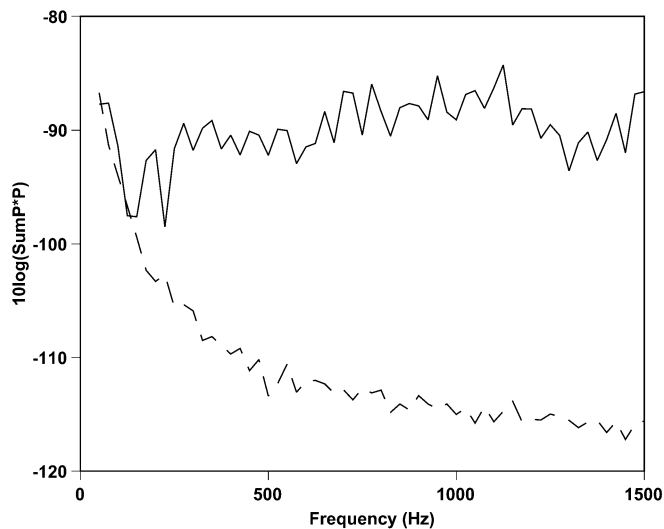
Fig. 9. Sum of the intensity overall depths in the water column at a range of 85 km for frequencies of 50–1500 Hz at 57 h. The solid curve is for the simulation with the internal wave present and the dashed curve is for the environment without the solitary internal-wave packet.

summed as a function of depth. This summation was done on a constant depth grid so as to avoid biasing the results. The sum is then converted to decibels to aid in plotting. The same process was done to the 57-h environment with the section containing the solitary internal wave removed. This result is shown in the lower curve in Fig. 9.

There are two points about this figure that are worthy of note. First, for the internal-wave environment, the energy does not fall off as a function of frequency as does the no-solitary wave case. In the latter case, the curve has a falloff with frequency that is more typically observed. One apparent acoustic effect of the solitary internal waves is the tendency to confine the acoustic energy within the water column and away from the absorbing bottom. Without the solitary wave the shelf bottom properties have a stronger effect on the acoustic energy propagating on the shelf. Second, for some frequencies there are indications of strong losses, e.g., at 175 and 225 Hz. This "resonance-like" effect is similar to the type of loss that Zhou *et al.* [6] found in the Yellow Sea. Note that there is no large dropout in acoustic intensity in the no-solitary wave case.

We have searched for a resonance effect by varying the acoustic source frequency and propagating the acoustic field through numerous environmental scenarios that represent several different realizations in the evolution of the solitary waves. As the acoustic field interacts with the solitary wave trains on the shelf, acoustic intensity redistribution can occur. Fig. 10 shows the resultant intensity for acoustic source frequencies of 450, 500, and 550 Hz, for a solitary wave train simulation that occurred at 55 h.

In Fig. 10(a), the two figures show the acoustic propagation loss contours (in decibels) for a 450-Hz acoustic source located at a depth of 125 m below the ocean surface at zero range. In the upper figure, the solitary wave packet is located between the ranges of 5 and 25 km. In the lower figure, the solitary wave packet is not included in the ocean environment. The lower figure indicates the acoustic propagation loss that would occur without the presence of the solitary wave packet. Note in the lower figure

that virtually no acoustic energy propagates beyond 70 km from the acoustic source. The effect of the solitary wave packet is to refract acoustic energy up and onto the shelf slope such that substantial acoustic energy propagates as far as 90 km from the acoustic source. This refracted energy can be viewed as acoustic mode conversions, from the deep-water acoustic modes into the shallow-water acoustic modes. Without the solitary wave packet no such mode conversions occur and the propagating shallow-water modes carry no substantial acoustic energy.

In Fig. 10(b), the ocean conditions are identical to that used in obtaining the results shown in Fig. 10(a). However, the acoustic source frequency has been increased from 450 to 500 Hz. Unlike the case shown for 450 Hz [Fig. 10(a)], the solitary wave packet here has only a slight acoustic effect and does not refract substantial acoustic energy up and into the shallow-water region shown on the right of the figures. This lack of refracted energy can be viewed as an indication that no significant acoustic mode conversions have occurred.

In Fig. 10(c), the ocean conditions are again identical to that used in obtaining the results shown in Fig. 8(a). However, the acoustic source frequency has been increased from 500 to 550 Hz. Similar to the 450 Hz case [Fig. 8(a)], the effect of the solitary wave packet at 550 Hz is to refract acoustic energy up and onto the shallow-water slope such that substantial acoustic energy propagates as far as 90 km from the acoustic source. This refracted energy can be viewed as acoustic mode conversions from the deep-water acoustic modes into the shallow-water acoustic modes. Without the solitary wave packet, no mode conversions occur and the shallow-water modes propagate no substantial acoustic energy.

The results shown in Fig. 10 are antithetic to the results reported by Zhou *et al.* [6] in that their results indicated that *near-surface* solitary internal waves could produce anomalous signal losses; their "normal environmental scenario" was no solitons present and no loss in signal; and their "anomalous environmental scenario" was solitons present and large signal losses within a narrowband of acoustic frequencies. In our case, we have *near-bottom* solitary internal waves producing anomalous signal gain; our "normal environmental scenario" is no solitons present and no significant signals detected on the shelf; and our "anomalous environmental scenario" is solitons present and large signal gains within a narrowband of acoustic frequencies detected on the shelf. We have observed similar signal gains in our coupled ocean-acoustic modeling studies of the Yellow Sea solitary waves [16]. In our Yellow Sea simulations, the near-surface solitary waves were dominant and signal losses due to acoustic mode conversions were observed similar to the results reported by Zhou *et al.* [6]. In addition to the signal losses observed at receiver depths below the thermocline, we also observed but did not report signal enhancement at receivers depths above the thermocline.

In this winter PRIMER study, we made a second set of model simulations using a shallow acoustic source. Some of the results of those calculations are shown in Fig. 11. For Fig. 11(a), the acoustic simulations were done for 56, 57, and 58 h. The environments are the same as that used in Fig. 8(a). For Fig. 11(b), the effect of the internal wave was removed and the calculations repeated. These calculations are based on the same environments as those used in Fig. 8(b). The difference is in the source
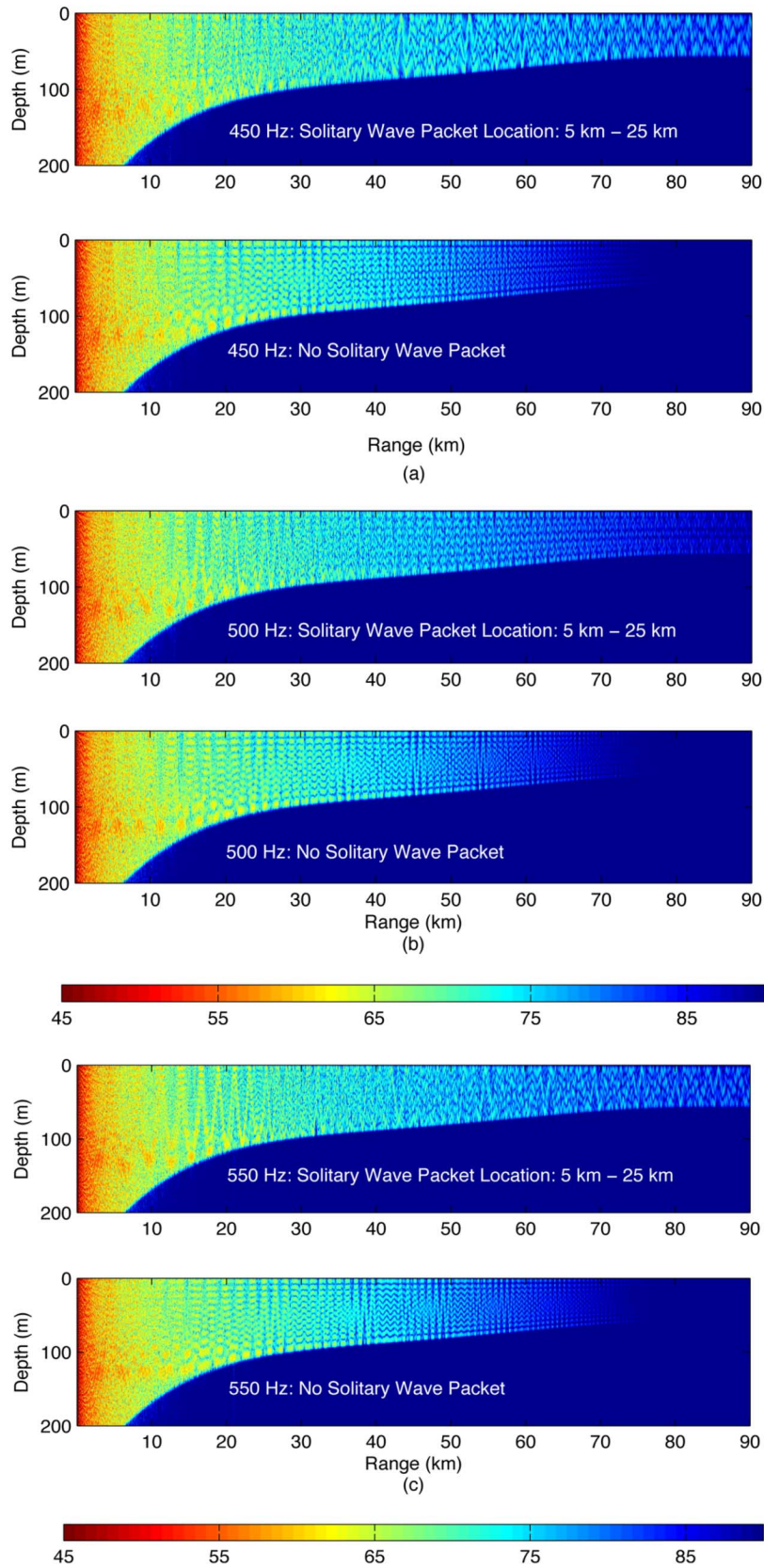
Fig. 10.   (a) Two figures show the acoustic propagation loss contours (in decibels) for a 450-Hz acoustic source located at a depth of 125 m below the ocean surface at zero range. In the upper figure, the solitary wave packet is located between the ranges of 5 and 25 km. In the lower figure, the solitary wave packet is not included in the ocean environment. The lower figure indicates the acoustic propagation loss that would occur without the presence of the solitary wave packet. Note in the lower figure that virtually no acoustic energy propagates beyond 70 km from the acoustic source. (b) Acoustic loss for 500 Hz with same configuration. (c) Acoustic loss for 550 Hz with same configuration. The shaded (color) scale at the bottom represents the loss in decibels with black (blue) the most intense and white (red) the least intense.
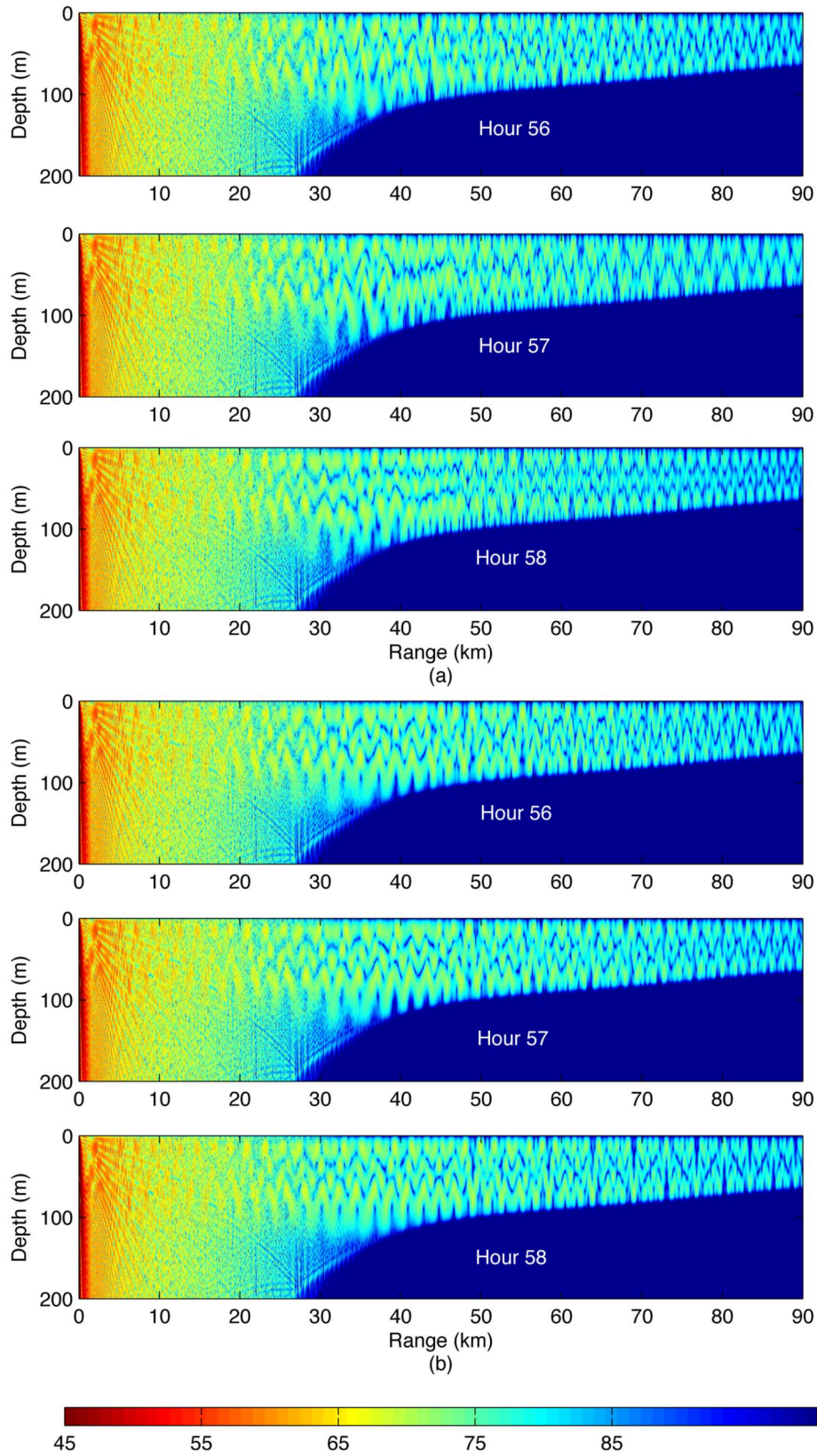
Fig. 11. Acoustic response to the environment for 56, 57, and 58 h. The acoustics are shown as transmission loss as a function of depth and range. The shaded (color) scale represents the loss in decibels with black (red) the most intense and white (blue) the least intense. The acoustic source is 225 Hz and is located at range of 0 km and a depth of 6 m. The simulations with internal waves present are shown in part (a) and the simulations without the internal waves are shown in part (b). The transmission loss seen in Fig. 8(a) at 57 h is not present in Fig. 11(a) due to the change in the source depth with the accompanying changes in the propagation paths. The shaded (color) scale at the bottom represents the loss in decibels with black (blue) the most intense and white (red) the least intense.

TABLE III
PHASE SPEED IN TIME

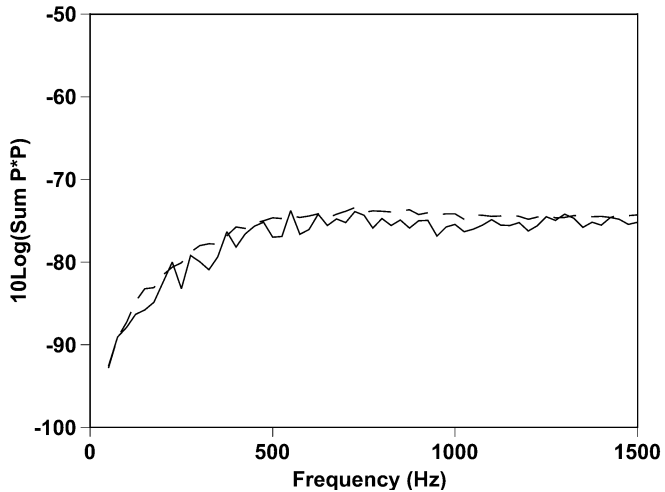| Time (h)	Peak velocity m/s at solitary waves			
	1	2	3	4
48-51	0.82	0.80	0.79	0.80
51-57	0.18	0.17	0.15	0.12
57-63	0.93	0.92	0.91	0.89
63-69	0.08	0.09	0.04	-
69-72	0.85	0.83	-	-
48-72	0.49	0.49	0.46	0.43

Fig. 12. Sum of the intensity overall depths in the water column at a range of 85 km for frequencies of 50–1500 Hz at 57 h. The source depth for this plot was set to 6 m. The solid curve is for the simulation with the internal wave present and the dashed curve is for the environment without the solitary internal-wave packet.

depth. For Fig. 8, the source depth was 125 m. For Fig. 11, the acoustic source was placed at a depth of 6 m. Thus, for the same environmental scenario the loss of acoustic energy shown in Fig. 8 is not seen in Fig. 11(a) where the only difference in the simulations is the acoustic source depth. Thus, the acoustic mode structure of the signal incident on the solitary internal-wave field is an important factor in the increased signal loss; the structure of the internal wave itself is the other important factor.

Fig. 12 shows the sum of the intensity over the water column for frequencies of 50–1500 Hz. The ocean environment is 57 h with an acoustic source depth of 6 m. The simulation was done with the internal wave present and with it removed. Note that with the near-surface source geometry the presence of the internal wave has much less effect on the received acoustic signal (in contrast to Fig. 9 where the acoustic source was at a depth of 125 m).

VII. CONCLUSION

The modeled dynamics of the semidiurnal–tidal motion over the shelfbreak generates depression waves that propagate to the right and to the left. The right propagating wave results in slight depression of the isopycnals. The left propagating wave results is a pronounced depression that moves up onto the shelf. Around the shelfbreak area, a mode-two structure can evolve.

Elsewhere a mode-one structure prevails. Nonlinear effects steepen the back side of the left propagating depression on the shelf. The front side flattens. Disintegration into solitary waves of elevation occurs through amplitude and frequency dispersion. After initial spin-up, one solitary wave train of elevation develops on the shelf every semidiurnal tidal period. As the trains propagate under the deep-winter mixed layer, the width of the solitons increases, the spacing between them increases, and attenuation in amplitude occurs. The picture is one of the near-bottom solitary waves on the shelf, moving and attenuating under the winter mixed layer.

The parameters of the model were derived from winter PRIMER4 data. The derived parameters were varied for the purpose of sensitivity studies. It was shown that an offshore current retards the motion of the internal bores, resulting in more steepening of the bores and a quicker disintegration into solitary waves through frequency and amplitude dispersion. Decreasing the amplitude of the barotropic semidiurnal tidal forcing by half results in less internal bore displacement and a reduction in nonlinear effect with fewer solitary waves. A decrease and increase of mixed-layer density generates a larger and smaller gradient in the pycnocline, respectively. This leads to the larger and smaller solitary wave phase speeds. Increasing the mixed-layer depth tends to suppress the solitary wave activity near the bottom of the shelf below the mixed layer.

The model simulations, with parameters obtained from measurements, were compared against observations at the thermistor chain mooring by placing an analogous mooring in the model domain. The amplitudes and periods of solitary wave trains were analyzed for three measured and three simulated time intervals. The modeled amplitudes and periods overlapped with the data, indicating that the model has skill. The overlap region contained amplitudes ranging from 7 to 27 m and periods from 0.25 to 0.5 h. The model represents local generation of internal solitary waves. The data contains locally generated solitary waves and, in addition, can contain solitary waves arriving from other generation sites.

Comparisons of time series spectra were conducted between the thermistor chain data and the corresponding observation mooring in the model. The variance spectra of the data and model moorings showed the presence of semidiurnal tidal and internal solitary wave energies. In addition, two other moorings were placed in the model domain, one 10 km to the right and another 10 km to the left. The analysis of model variance spectra at the three moorings exhibits a conversion of energy from the semidiurnal tidal band to the internal solitary waves band as one moves up onto the shelf through the three moorings. The internal solitary wave energy increases and the semidiurnal tidal energy decreases. This indicates energy conversion from the barotropic tide to the baroclinic tide and into internal solitary waves.

Calculation of acoustic intensity in conjunction with model-predicted solitary wave train structures on the shelf indicate significant fluctuations of acoustic intensity in the spatial and temporal bands due to the presence of the solitary waves. In some cases, these fluctuations in acoustic intensity are similar to that observed by Zhou et al. [6], resulting in anomalous signal losses; however, in other cases these fluctuations can produce significant gains in acoustic intensity. Our simulations indicate

that significant acoustic energy from an omnidirectional point source located at depths more than twice the shelf depth can, nevertheless, propagate onto the shelf region via refraction paths (i.e., acoustic mode conversions) caused by the internal-wave environment. Such anomolous signal gains stand in contrast to the more commonly discussed anomolous signal losses caused by solitary internal waves.

REFERENCES

[1] A. Newhall, K. V. D. Heydt, B. Sperry, G. Gawarkiewicz, and J. Lynch, Preliminary acoustic and oceanographic observations from the winter primer experiment Woods Hole Oceanic Inst.,, Tech. Rep. WHOI-98-19, Oct. 1998.

[2] G. T. Csanady and P. Hamilton, "Circulation of slopewater," *Continental Shelf Res.*, vol. 7, no. 5–7, pp. 565–624, 1988.

[3] R. C. Beardsley, D. C. Champman, K. H. Brink, S. R. Ramp, and R. Schlitz, "The Nantucket shoal flux experiment. Part A. A basic description of the current and temperature variability," *J. Phys. Oceanogr.*, vol. 15, no. 6, pp. 713–748, 1985.

[4] P. Baines, "The generation of internal tides by flat-bump topography," *Deep Sea Res.*, vol. 20, pp. 179–205, 1973.

[5] P. Baines, "On internal tide generation models," *Deep Sea Res.*, vol. 29, pp. 307–338, 1982.

[6] J. X. Zhou, X. Z. Zhang, and P. H. Rogers, "Resonant interaction of sound wave with internal solitons in the coastal zone," *J. Acoust. Soc. Amer.*, vol. 90, pp. 2042–2054, 1991.

[7] T. J. Sherwin, "A numerical investigation of semi-diurnal fluctuations in acoustic intensity at a shelf edge," in *Ocean Variability and Acoustic Propagation*, J. Potter and A. Warn-Varnas, Eds. Norwell, MA: Kluwer, 1991, pp. 579–592.

[8] J. C. Preisig and T. F. Duda, "Coupled acoustic mode propagation through continental-shelf internal solitary waves," *IEEE J. Ocean. Eng.*, vol. 22, no. 2, pp. 256–269, Apr. 1997.

[9] T. F. Duda and J. C. Preisig, "A modeling study of acoustic propagation through moving solitary-wave packets," *IEEE J. Ocean. Eng.*, vol. 24, no. 1, pp. 16–32, Jan. 1999.

[10] S. Finette, M. H. Orr, A. Turgut, J. R. Apel, M. Badiey, C.-S. Chiu, R. H. Headric, J. N. Kemp, J. F. Lynch, A. E. Newhall, K. V. D. Heydt, B. H. Pasewark, S. N. Wolf, and D. Tielbuerger, "Acoustic field variability induced by time evolving internal wave fields," *J. Acoust. Soc. Amer.*, vol. 108, pp. 957–972, 2000.

[11] O. C. Rodriquez, S. Jesus, Y. Stephan, X. Demoulin, M. Porter, and E. Coelho, "Nonlinear soliton interaction with acoustic signals: Focusing effects," *J. Comput. Acoust.*, vol. 8, pp. 347–363, 2000.

[12] A. C. Warn-Varnas, S. A. Chin-Bing, D. B. King, Z. Hallock, and J. A. Hawkins, "Ocean-Acoustic solitary wave studies and predictions," *Surveys Geophys.*, vol. 24, pp. 39–79, 2003.

[13] J. A. Colosi, J. F. Lynch, R. Beardsley, G. Gawarkewicz, A. Scotti, and C. S. Chiu, "Observations of nonlinear internal waves on the outer New England continental shelf during the summer shelfbreak PRIMER study," *J. Geophys. Res.*, vol. 106, no. (C5), pp. 9587–9601, 2001.

[14] K. Lamb, "Numerical experiments of internal wave generation by strong tidal flow across a finite amplitude bank edge," *J. Geophys. Res.*, vol. 99, pp. 848–864, 1994.

[15] M. D. Collins, "Benchmark calculations for higher-order parabolic equations," *J. Acoust. Soc. Amer.*, vol. 87, pp. 1535–1538, 1990.

[16] S. A. Chin-Bing, A. Warn-Varnas, D. B. King, K. G. Lamb, M. Teixeira, and J. A. Hawkins, "Analysis of coupled oceanographic and acoustic soliton simulations in the Yellow Sea: A search for soliton-induced resonances," *Math. Comput. Simul.*, vol. 62, pp. 11–20, 2003.

[17] T. F. Duda, "Acoustic mode coupling by nonlinear internal wave packets in a shelfbreak front area," *IEEE J. Ocean. Eng.*, vol. 29, no. 1, pp. 118–125, Jan. 2004.

Alex C. Warn-Varnas received the B.S. degree in physics from the University of Illinois at Chicago, Chicago, in 1960, the M.S. degree in physics from DePaul University, Chicago, IL, in 1963 and the Ph.D. degree in geophysical fluid dynamics from the University of Notre Dame, Notre Dame, IN, in 1969.

Over the past 36 years, his career involved engineering work at National Aeronautics and Space Administration (NASA) and General Dynamics and Astronautics, radiation physics at the University of Illinois IRE Hospital, and teaching at the University of Illinois College of Pharmacy. He was an Associate on rotating annulus simulations of Geophysical Fluid Dynamics Institute (GFDI), Florida State University, Tallahassee. His research included physics of collapsing mixed regions at the Naval Research Laboratory (NRL), Washington, DC. He was a Section Head of Upper Ocean Analysis and Prediction at Naval Ocean Research and Development Activity (NORDA) where upper ocean prediction evolved, a Visiting Associate Professor on the level of no motion reference at the University of Chicago, and a Visiting Scholar on multiyear ice cycles at Northwestern University, Evanston, IL. He was also a Branch Head of Hydrodynamics and Thermodynamics at NORDA where operational ice prediction evolved, a Head of Applied Oceanography Department at NATO's SACLANT Undersea Research Centre where he evolved with colleagues rapid assessment of the mesoscale in the ocean. Currently, He is an Oceanographer at the Stennis Naval Research Laboratory where he develops internal-wave prediction. He has worked jointly on projects with colleagues at Dartmouth College, Woods Hole Oceanographic Institution (WHOI), SCRIPPS, Harvard University, University of Massachusetts, University of Waterloo, and the Polytechnic University of Puerto Rico. He has authored and coauthored numerous publications on his work. His interests include internal waves from a cross-disciplinary approach involving joint ocean-acoustic studies and predictions, linking oceanographic and acoustic parameters, ocean model optimization using acoustic modes, water mass and feature models for mesoscale prediction, and rapid assessment and prediction of the ocean.

Dr. Warn-Varnas is a Member of the American Geophysical Union, European Geophysical Society, Sigma Xi, Oceanographic Society, and the American Acoustical Society.

Stanley A. Chin-Bing (M'02) was born in New Orleans, LA, on November 3, 1942. He received the B.S. degree in physics from Tulane University, New Orleans, LA, in 1964, and the M.S. and Ph.D. degrees in physics from the University of New Orleans, New Orleans, in 1968 and 1973, respectively.

From 1968 to 1969, he worked for the Chrysler Corporation Space Division, from 1974 to 1975, at the Martin Marietta Corporation, and from 1976 to 1977, at the Chrysler Corporation Defense Division. His U.S. Navy research career spans nearly 30 years including Naval Ocean Research and Development Activity from 1978 to 1988, the Naval Oceanographic and Atmospheric Research Laboratory from 1988 to 1992, and he has been working at the Naval Research Laboratory (NRL) since 1992, where he is currently a Supervisory Research Physicist and a Branch Head in the Acoustics Division. His research speciality is ocean-acoustic propagation modeling. Concurrent with his U.S. Navy research career, he has held the position of Adjunct Professor of Physics at the University of New Orleans, where he has developed and taught nine different graduate courses in acoustics.

Dr. Chin-Bing is a Fellow of the Acoustical Society of America.

David B. King received the Ph.D. degree in physics from the University of New Orleans, New Orleans, LA, in 1979.

Upon graduation, he joined the acoustic division of the Naval Research and Development Activity at Stennis Space Center, MS, as a Research Physicist. This group, after a couple of reorganizations, was absorbed into the Naval Research Laboratory (NRL) as the Acoustic Simulation, Measurement, and Tactics Branch of NRL's Acoustics Division. He has been with this group for over 26 years working various aspects of acoustic modeling. His current areas of work include coupling of oceanographic models and acoustic models, benchmarking of acoustic models, inversion of acoustic/geophysical data and high-fidelity acoustic modeling.
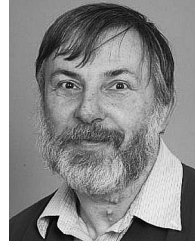
James A. Hawkins was born in Pasadena, TX, on August 23, 1950. He received the B.A. degree in biology from the University of Texas, Austin, in 1974, the M.S. degree in physical science from the University of Houston, Clear Lake City, TX, in 1980, the M.A. degree in physics from the University of Texas, Austin, in 1987, and the Ph.D. degree in mechanical engineering from the University of Texas, Austin, in 1992.

He worked at the Naval Research Laboratory (NRL), Stennis Space Center, MS, from 1993 to 1995. He then worked at Texas A&M University, College Station, from 1995 to 1999, after which he joined Planning Systems Incorporated, Slidell, LA, where he currently works. His background is primarily ocean acoustics and he is currently working on physical oceanography projects including coupled ocean-acoustic studies.

James F. Lynch (M'96–SM'03–F'05) was born in Jersey City, NJ, on June 3, 1950. He received the B.S. degree in physics from Stevens Institute of Technology, Hoboken, NJ, in 1972 and the Ph.D. degree in physics from the University of Texas at Austin, in 1978.

From 1978 to 1981, he worked at the Applied Research Laboratories, University of Texas at Austin (ARL/UT), after which he joined the scientific staff at the Woods Hole Oceanographic Institution (WHOI), Woods Hole, MA. He has worked at WHOI since then, and currently holds the position of a Senior Scientist in the Applied Ocean Physics and Engineering Department. His research specialty areas are ocean acoustics and acoustical oceanography, but he also greatly enjoys occasional forays into physical oceanography, marine geology, and marine biology.

Dr. Lynch is a Fellow of the Acoustical Society of America.

Kevin G. Lamb received the B.Math. degree in applied and pure mathematics from the University of Waterloo, Waterloo, ON, Canada, in 1985 and the Ph.D. degree in the Program in Applied and Computational Mathematics from Princeton University, Princeton, NJ, in 1989.

He was a Faculty Member in the Department of Physics and Physical Oceanography at the Memorial University of Newfoundland, St. John's, NL, Canada, from 1989 until 1997 when he joined the Department of Applied Mathematics at the University of Waterloo. His current interests are in nonlinear internal gravity waves, surface waves, and hydrodynamic stability.